International Journal of Engineering Inventions
e-ISSN: 2278-7461, p-ISSN: 2319-6491
Volume 13, Issue 5 [May. 2024] PP: 110-116

Innovative Design and Implementation of a Six-Degree-of-Freedom Stewart Platform for Enhanced Patient Comfort in Ambulance Stretchers.

1. **Mr.N.SRINIVASAN**, *PG Student, Department Of Mechanical Engineering, Vinayak Missions kirupanandavariyar Engineering College,Salem,Taminadu,India,natarajanshree@gmail.com.*
2.**Dr.S.NATARAJAN**,*Professor,department of mechanical engineering, Vinayak Missions kirupanandavariyar Engineering College,Salem,Taminadu,India,natarajanshree@gmail.com.*
3. **Dr.V.NARESH**, *Associate professor, Bharathidasan Engineering College,Nattrampalli,nareshmeed@gmail.com*

Abstract
This research paper explores the development and application of a cutting-edge Stewart platform with six degrees of freedom (6-DOF) integrated into ambulance stretchers to optimize patient comfort during transportation. The Stewart platform, known for its exceptional stability and maneuverability, is adapted to address the unique challenges faced by patients in emergency medical situations. The study delves into the mechanical design, kinematics, and control system of the platform, emphasizing its ability to provide precise and adaptable motion for ambulance stretchers. The incorporation of the 6-DOF Stewart platform aims to mitigate the discomfort experienced by patients during ambulance transit, particularly in cases of uneven terrain or sudden movements. Through comprehensive simulations and prototype testing, the research evaluates the platform's performance in terms of stability, responsiveness, and overall patient well-being. The study also investigates the potential impact on emergency medical personnel and their ability to administer care during transportation.
Keyword:

Date of Submission: 05-05-2024 Date of acceptance: 17-05-2024

I. INTRODUCTION

Motions robots perform during a robotic operation in space can be divided into gross motion and fine motion. Gross motion permits low positioning accuracy, e.g. in obstacle avoidance, while fine motion requires very high positioning accuracies, usually of thousands of an inch, e.g. in mating and demating space-rated connectors. Traditional robot manipulators are anthropomorphic open-kinematic chain (OKC) mechanisms whose joints and links are actuated in series. OKC manipulators generally have long reach, large workspace and are capable of entering small spaces because of their compactness. However, their cantilever-like structure causes OKC manipulators to have low stiffness and consequently undesirable dynamic characteristics, especially at high speed and large payload. In addition, they have low strength-to-weight ratios due to the fact that the payload is not uniformly distributed to the actuators. Finally, the fact that relatively large position error occurs at the last link because the joint errors are accumulated throughout the mechanism suggests that OKC manipulators are not suitable for high-precision tasks. As a result, it was proposed in that a robotic end-effector capable of performing high-precision motion be mounted to a general OKC manipulator to perform fine motion while the OKC manipulator is solely responsible for carrying out gross motion during a telerobotic operation. Closed-kinematic chain (CKC) mechanism has been selected for the design of the end-effector because even though it has relatively small workspace and low maneuverability, it possesses high positioning capability produced by its high structural rigidity and noncumulative actuator errors. CKC mechanism also has higher strength-to-weight ratios as compared to the OKC mechanism because the payload is proportionally distributed to the links. In addition, the inverse kinematic problem of the CKC mechanism has simple closed-form solutions. Implementations of the CKC mechanism concept first appeared in the Stewart Platform which was originally designed as an aircraft simulator. A typical Stewart Platform consists of two platforms driven by a number of parallel actuators and is often referred as parallel mechanism or parallel manipulator. The invention of the Stewart Platform has attracted tremendous robot designer's attention and its mechanism was used in many robotic applications.

Recently a robotic wrist possessing 6 DOFs was designed and built at the Goddard Space Flight Center (NASA) based on the mechanism of the Stewart Platform to serve as a tested for studying high-precision robotic operations in space. This paper presents the development and implementation of kinematic transformations for the robotic wrist. This paper is organized as follows. The next section describes the main components of the robotic wrist. Then a kinematic analysis is performed to provide a closed-form solution to the inverse kinematic transformaction. After that, a computationally efficient solution is derived for the forward kinematic transformation using the Newton-Raphson method which simultaneously provides a modified Jacobian matrix. Finally evaluation of the forward kinematic transformation and modified Jacobian matrix is done by means of a computer simulation whose results are presented and discussed.

1. THE STEWART-PLATFORM BASED ROBOTIC WRIST

presents a robot manipulator of the Intelligent Robotic Laboratory (IRL) at the Goddard Space Flight Center (NASA), which consists of a 6 DOF Cincinnati T3 robot and a 6 DOF Stewart Platform-based robotic wrist mounted to the last link of the T3 robot. The manipulator has a total of 11 DOFs since 1 DOF of the wrist is identical to that of the T3 robot. The main function of the T3 robot is to perform gross motion, for example to bring the robotic wrist into its workspace and then let the wrist carry out fine motion required for high-precision operations such as assembly of parts, mating connectors, etc. As shown in Fig. 2, the design of the robotic wrist is based on the mechanism of the Stewart Platform. It mainly consists of a payload platform, a base platform, six linear actuators and a gripper attached to the payload platform. The payload platform is coupled with the base platform by the actuators each of which is composed of a NSK ballscrew assembly mounted axially with a PMI d.c. motor. The motors drive the ballscrews to extend or shorten the actuator lengths whose variations will in turn produce the motion of the payload platform relative to the base platform. The actuator lengths are measured by six BALLUFF linear displacement transducers (LDT) mounted along the actuators. Forces/torques exerted by the gripper are acquired through a JR 3 Universal Force-Moment Sensor System mounted between the gripper base and the payload platform. Each end of the acuator links is mounted to the platforms by 2 DOF universal joints. The LDT signals are sent to the IRL local area network (LAN) via an ethernet board and a data translation input board resided in a PC/386. An Apollo workstation will take the sensor signals off the LAN by means of another ethernet board, performs all necessary computations for the implementation of control schemes, coordinate transformations, etc., and sends the actuating signals to the PMI motor drives via a data translation output board.

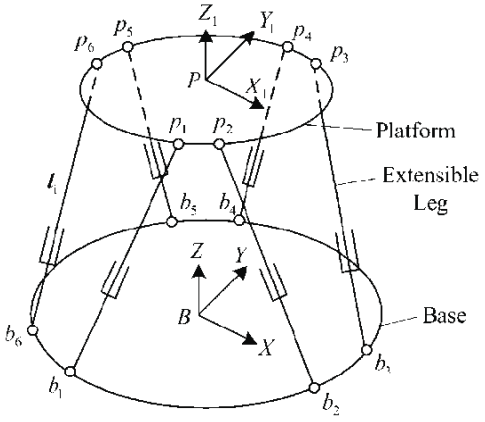

2. Identification process

The above analysis of the identification principle based on sinusoidal vibrations provides a solid foundation for a novel identification process. The steps of the identification approach are summarized as follows: (a) Excite the system in each of the six DOFs independently. In this step, the test frequency of the ground harmonic xt should be chosen below the lowest open loop ‘rigid’ eigen frequency to avoid exciting relevant parasitic flexible modes of the system. Amplitudes of required harmonic reference signals should be chosen properly to minimize nonlinear effects caused by sx and to moderate the exciting energy used for identification. (b) Preprocess data. The platform position Spi is obtained using the forward kinematics solution and length signals of measurement actuators li. The platform force in the task space Sfi is calculated as F ¼ JT lxðsxÞfai, where fai is the force signals of the measurement actuator.

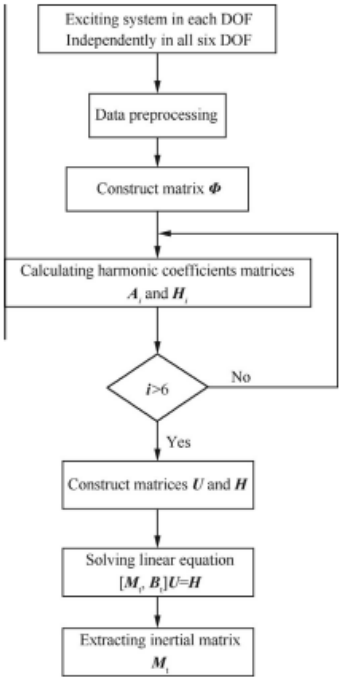

Flowchart of identification approach.

Method A

In the case of employing Method A, the maximum identified error is the difference between Ixx and Iyy, which is 3.4 kgÆm2 and almost equal to the difference in the case of employing Method B (3.0 kgÆm2). Comparing with the inertial matrix identified using the nonlinear friction simulation model, it is found that the changing trends of the two inertial matrices are similar; e.g., the cross terms (Mt (1,5), Mt (2,4), Mt (4,2) and Mt (5,1)) become inaccurate, the identified value of mz is lower than the nominal value, and mx and my and Ixx and Iyy are not equal in the identified inertial matrix. Hence, dry friction must be regarded when the dynamic parameters of the real parallel manipulator are identified. In this situation, a modified identification coupling parameter of 27.75 kgÆm can be obtained using the modified formula proposed in this paper. Comparing with the identified values identified using the Modified Method A and the nominal values which are obtained from analytic formula, it is found that (1) For mass parameters of inertial matrix ðmx; my ; mzÞ, the maximum identification error is 6.3 kg, 2.3%. (2) For inertial parameters of inertial matrix ðI xx; I yy ;IzzÞ, the maximum identification error is 1.6 kgÆm2 , 6.4%. (3) For the cross terms (Mt (1,5), Mt (2,4), Mt (4,2) and Mt (5,1)), the identification error is 12.52 kgÆm, 82%. By analyzing the error of data between analytic formula and experiments result, we found that the identification error increases with inertial effects increasing caused by the actuators in identified inertial values. Especially for the cross terms, the max identification error is 82%, which is much larger than the identification error of mass and inertial parameters of inertial matrix. The essential reason is the uncertainty on the dynamic parameters of actuators ðia; ib; ma; mb;ra;rbÞ between CAD model and experimental platform. The nonlinear friction effect on dynamic-parameter identification will be further studied in future work This paper takes into consideration multiple influential factors of the measurement accuracy of the interaction forces between components. Among the forces, gravity is of great research interest, and for the first time, this paper provides an analytical algorithm of a six-dimensional F/T with dynamic gravity compensation. The setup of the paper is as follows: Section 1 introduces the digital flexible assembly system and its significance, highlights the applications of the SP, and provides a new perspective and novel methods of large components alignment. Section 2 provides the analytical algorithm of a six-dimensional F/T, proposes a dynamic gravity compensation model based on the screw theory, and offers a parameter which is optimized through experiments. For the spatial precision analysis, Section 3 uses an approximate cone shape to evaluate the accuracy and repeatability of the sixdimensional F/T. In Section 4, using the designed P&O adjusting platform to verify the accuracy of the proposed algorithm and perform spatial precision experiments, relevant experimental data are analyzed and discussed. Section 5 concludes the paper and assesses the validity and limitations of the present algorithm and model.

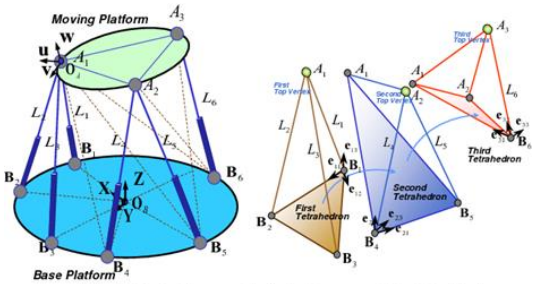

The 3-6 platform with 3-2-1 type and its tetrahedron configurations.

Method B

The estimated inertial matrix is given in Table , where the identified values of Method A, Modified Method A and Method B are obtained from the experiment, and the nominal value of inertial matrix Mt is obtained from analytic formula. The inertial matrix becomes almost diagonal owing to the platform's main axes of inertia being set along the platform frame axes, and the cross term mqz (Mt (1,5), Mt (2,4), Mt (4,2) and Mt (5,1)) results from the center of gravity not coinciding with the origin of the moving body frame. In principle, the nominal inertial matrix should be symmetric, which means Mt (1,5) = Mt (5,1) = mqz, Mt (2,4) = Mt (4,2) =

---

mqz and mz > mx ¼ my;Izz > Ixx ¼ Iyy when the inertial effects of all the actuators are considered. The difference between the nominal inertial matrix and identified inertial matrix can give some impression of the errors resulting from nonlinear terms. The difference between mx and my is 2 kg when employing Method A but 6.6 kg when employing Method B.

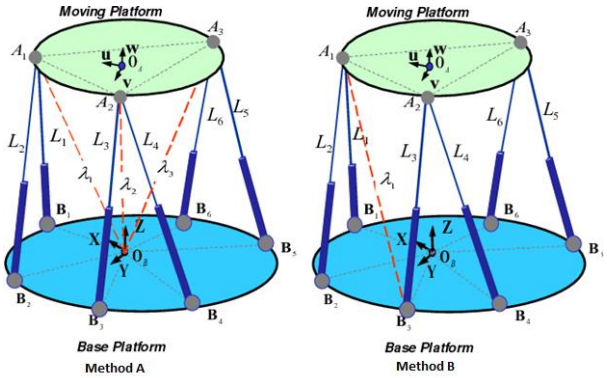

However, for force signals, nonlinear terms are more complex than those in the simulation. Higher harmonic signal components are caused by not only the Coriolis–centrifugal force and dry friction but also a pressure jump in the commutation of the asymmetric hydraulic cylinder25 and the dynamics of the long-stroke hydraulic pipeline that we do not considered in the simulation model.

Then the inertial matrix $\boldsymbol{M}_t$ can be written as

$$\boldsymbol{M}_t = \begin{bmatrix} m_x & 0 & 0 & 0 & -m_{\rho z} & 0 \\ 0 & m_y & 0 & m_{\rho z} & 0 & 0 \\ 0 & 0 & m_z & 0 & 0 & 0 \\ 0 & m_{\rho z} & 0 & I_{xx} & 0 & 0 \\ -m_{\rho z} & 0 & 0 & 0 & I_{yy} & 0 \\ 0 & 0 & 0 & 0 & 0 & I_{zz} \end{bmatrix} \quad \text{(A9)}$$

where

$$m_x = m_y = m + 3\left(m_a\left(1 - l_{n1z}^2\right) + m_{imab}\left(1 + l_{n1z}^2\right)\right),$$

$$m_z = m + 6\left(m_a l_{n1z}^2 + m_{imab}\left(1 - l_{n1z}^2\right)\right),$$

$$I_{xx} = I_{cxx} + 3\left(m_{imab}\left(a_{1x}^2 + a_{1y}^2 + 2a_{1z}^2 - \left(v_{1y}^2 + v_{1z}^2\right)\right) + m_a\left(v_{1x}^2 + v_{1y}^2\right)\right),$$

$$I_{yy} = I_{cyy} + 3\left(m_{imab}\left(a_{1x}^2 + a_{1y}^2 + 2a_{1z}^2 - \left(v_{1y}^2 + v_{1z}^2\right)\right) + +m_a\left(v_{1x}^2 + v_{1y}^2\right)\right),$$

$$I_{zz} = I_{czz} + 6\left(m_{imab}\left(a_{1x}^2 + \mathrm{a}_{1y}^2 - v_{1z}^2\right) + m_a v_{1z}^2\right),$$

$$m_{\rho z} = 3\left(m_{imab}\left(l_{n1x}v_{1y} - l_{n1y}v_{1x} - 2a_{1z}\right) - m_a\left(l_{n1x}v_{1y} - l_{n1y}v_{1x}\right)\right).$$

3. Optimization design result analysis of dual-degree-of-freedom magnetic levitation vibration energy harvester

Considering that the acceleration range of bridge vibration brought by vehicles is 0.5 m/s2 -1.5 m/s2 , the excitation amplitude generated by simple harmonic vibration should be set to 1 m/s2 . Combined with the application experience of NSGA-II algorithm in the industry and the characteristics of this axle vibration data, after several debugging, the target parameters, design variables, constraints, population size, number of iteration steps, the crossover coefficient, and the coefficient of variation in NSGA-II algorithm are taken as 2, 9, 2, 100, 200, 0.8, and 0.4, respectively, To increase the comparative value of the study, the SMEH is now used to construct a comparative parameter optimization model according to the same algorithm. The parameters of the SMEH optimization design model are selected in the same way as those of the DMEH. Three concrete simply supported girder bridges of different sizes were selected for the study to assist the optimized design of the vibration energy harvester, and to simplify the description, the abbreviations CSSBB1, CSSBB2, and CSSBB3 were given, and the basic information of the three simply supported girder bridges is shown in Table 1. In addition, each type of simply supported girder bridge. The mathematical models of NSGA-II algorithm, SMEH and DMEH are written in Python language, and the data of the optimal solution set after the optimization of each model is completed are counted to obtain . respectively show the Pareto optimal solution set distribution of simply supported beam bridges CSSBB1, CSSBB2, and CSSBB3 using two vibration energy harvesting models: DMEH and SMEH. The horizontal and vertical axes in Fig. 6 show the negative number of the probability in the maximum output and the total volume of the minimum magnet, respectively, and the icons of different colors represent different energy harvester models. Analysis of Fig. 6 shows that after both models have completed the optimization calculation

PARAMETER	METHOD A		METHOD B		NOMINAL VALUE	PLACE IN INERTIAL MATRIX Mt
	IDENTIFIED VALUE	ERROR (%)	IDENTIFIED VALUE	ERROR (%)		
Mx(kg)	272.42	012	252.72	7.17	272.10	(1,1)
My(kg)	272.42	012	252.62	7.14	272.10	(2,2)
Mz(kg)	272.42	011	272.45	0.11	272.11	(3,3)
Ixx(kg.m^2)	30.65	0.45	23.41	23.98	30.79	(4,4)
Iyy(kg.m^2)	30.65	0.45	23.42	23.97	30.79	(5,5)
Izz(kg.m^2)	53.49	0.40	54.49	0.40	53.28	(6,6)
Mt(1,5)(kg.m)	15.30	0.53	11.21	32.91	15.22	(1,5)
Mt(2,4)(kg.m)	-15.30	0.54	-11.12	32.91	-15.22	(2,4)
Mt(4,2)(kg.m)	-14.30	0.53	22.03	244.73	-15.22	(4,2)
Mt(5,1)(kg.m)	14.30	0.53	-22.03	244.73	14.22	(5,1)

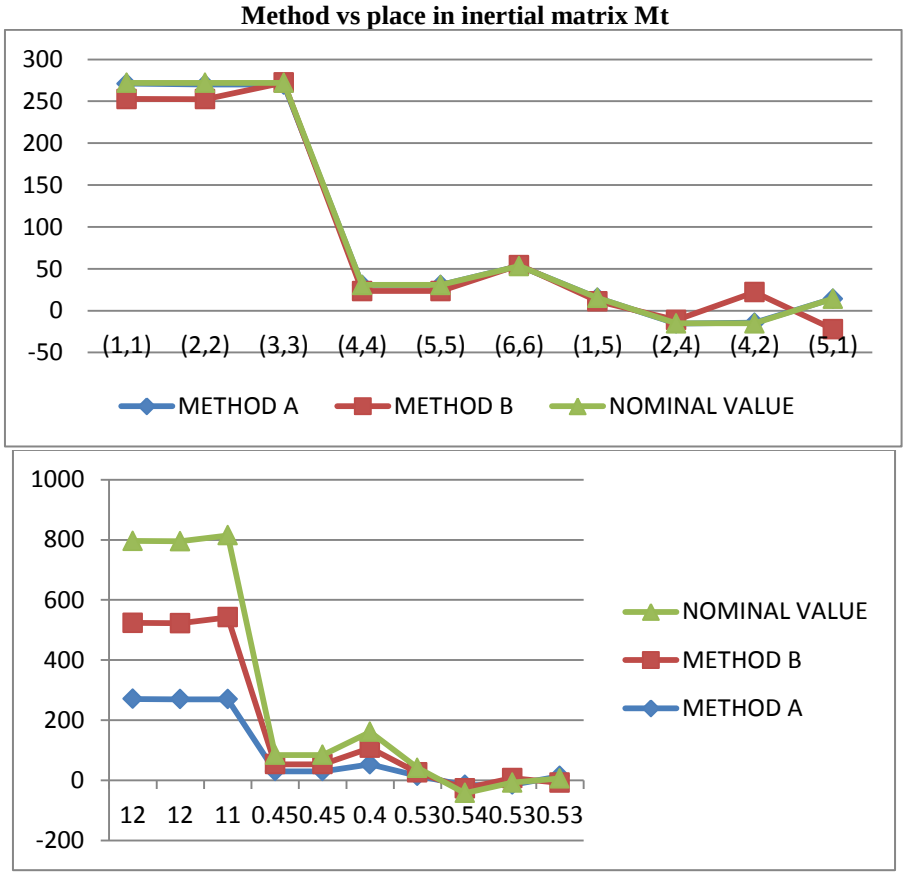

Methods Vs Error (%)

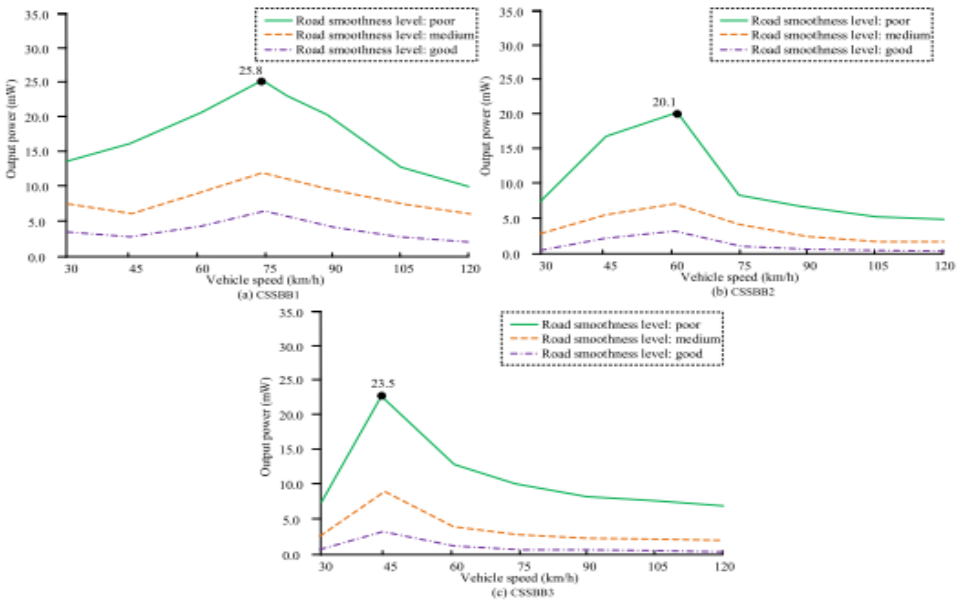

Comparison of total output power of SMEH under different road surface roughness conditions.

A compact identification process that allows estimation of the relevant dynamic parameters of the six-DOF parallel manipulator through identifying a (6 · 6) inertial matrix from the results of six persistently exciting periodic motion tests is proposed in this paper. By solving linear equations based on the ground harmonic of sinusoidal vibrations, velocity-related (friction) and higher order terms (nonlinearities) have minimal effect on the procedure. The proposed identification procedure is validated initially by considering a simulated parallel

manipulator for which linear and nonlinear friction models are applied to passive and active joints, respectively. The obtained results show that the new identification procedure is able to handle the coupling phase shift associated with the cross term of viscous friction and can tolerate dry friction using a modified formula with a simple coupling parameter. An experiment is carried out to identify the dynamic parameters of an actual manipulator of this structure. The effect of nonlinear friction in parameter identification is demonstrated by comparing an inertial matrix obtained from experimental results and a nonlinear friction simulation model. In particular, the proposed identification process can be applied to any parallel manipulator or closed-link mechanism.

II. Conclusion

In order to improve the performance of vibration energy harvester using bridge vibration energy generation, this study designed a six-degree-of-freedom magnetically levitated vibration energy harvester and designed an energy conversion mathematical model for DMEH, and then used NSGA-II algorithm to optimize the structural parameters of DMEH. The experimental results show that the maximum total output power of DMEH and SMEH on CSSBB1, CSSBB2 and CSSBB3 are 48.7 mW, 36.8 mW, 25.4 mW and 27.2 mW, 21.5 mW, 14.9 mW, respectively, and the minimum total magnet volumes of both on CSSBB1, CSSBB2 and CSSBB3 are 268 cm3 , 132 cm3 , 219 cm3 and 214 cm3 , 86.2 cm3 , 156 cm3 . The maximum total output power and corresponding driving speed of DMEH on CSSBB1, CSSBB2 and CSSBB3 are 31.2 mW, 28.9 mW, 31.5 mW and 75 km/h, 60 km/h and 45 km/h respectively. SMEH The maximum total output power and corresponding driving speed on CSSBB1, CSSBB2 and CSSBB3 are 25.8 mW, 20.1 mW, 23.5 mW with 75 km/h, 60 km/h, 45 km/h. The total output power of DMEH is greater than SMEH under various road leveling conditions. When the road leveling is “poor", the maximum total output power of DMEH is 6.0 mW, 8.8 mW and 8.0 mW higher than that of SMEH, respectively. On the whole, if ignoring the vehicle driving speed, the variation of total output power of DMEH is larger than that of SMEH, and the median, maximum and minimum values are larger than that of SMEH. Specifically, the median total power output of DMEH and SMEH under the conditions of “good”, “medium” and “poor” road leveling are 4.7 mW, 10.1 mW, 18.5 mW and 10.1 mW, respectively, From the experimental data, it can be seen that the maximum output power of the optimal solution of DMEH is significantly larger than that of SMEH for the selected simply supported girder bridge project, and the volume of the former is larger than that of the latter, but the degree of increase can still be adapted to the application environment

References

[1]. P. Han, G. Pan, B. Zhang, W. Wang, W. Tian, Three-cylinder oscillator under flow: flow induced vibration and energy harvesting, Ocean Eng. 211 (2020), 107619.1-107619.17.

[2]. S. Shaaban, Enhancement of the solar trough collector efficiency by optimizing the reflecting mirror profile, Renew. Energy 176 (2021) 40–49.

[3]. M. Zhang, C. Zhang, A. Abdelkefi, H. Yu, O. Gaidai, X. Qin, H. Zhu, J. Wang, Piezoelectric energy harvesting from vortex-induced vibration of a circular cylinder: effect of Reynolds number, Ocean Eng. 235 (2021), 109378.1-109378.13.

[4]. C. Liu, R. Zhao, K. Yu, H.P. Lee, B. Liao, A quasi-zero-stiffness device capable of vibration isolation and energy harvesting using piezoelectric buckled beams, Energy 233 (2021), 121146.1-121146.18.

[5]. E. Masero, J.M. Maestre, E.F. Camacho, Market-based clustering of model predictive controllers for maximizing collected energy by parabolic-trough solar collector fields, Appl. Energy 306 (2022), 117936.1-117936.12.

[6]. X. Liu, C. Sun, Y. Wang, F. Jiang, C. Zhang, Vibration characteristic analysis of transformers influenced by DC bias based on vibration half-wave energy method, Int. J. Electr. Power Energy Syst. 128 (4) (2021), 106725.1-106725.8.

[7]. Z.Q. Lu, D. Wu, H. Ding, L.Q. Chen, Vibration isolation and energy harvesting integrated in a Stewart platform with high static and low dynamic stiffnessScienceDirect, Appl. Math. Model. 89 (Pt. 1) (2021) 249–267.

[8]. H. Zhang, X. Xiang, B. Huang, Z. Wu, H. Chen, Static homotopy response analysis of structure with random variables of arbitrary distributions by minimizing stochastic residual error, Comput. Struct. 288 (2023) 107153.

[9]. J. Wang, F. Liang, H. Zhou, M. Yang, Q. Wang, Analysis of position, pose and force decoupling characteristics of a 4-ups/1-rps parallel grinding robot, Symmetry 14 (4) (2022) 825.

[10]. K. Liao, D. Lu, M. Wang, J. Yang, A low-pass virtual filter for output power smoothing of wind energy conversion systems, IEEE Trans. Ind. Electron. 69 (12) (2022) 12874–12885.

[11]. M. Chen, X. Zhang, J. Liu, F. Liu, R. Zhang, P. Wei, H. Feng, M. Tu, A. Qin, W.Y. Lam, D. Ding, B.Z. Tang, Evoking photothermy by capturing intramolecular bond stretching vibration-induced dark-state energy, ACS Nano 14 (4) (2020) 4265–4275.

[12]. J. Wang, L. Tang, L. Zhao, G. Hu, R. Song, K. Xu, Equivalent circuit representation of a vortex-induced vibration-based energy harvester using a semi-empirical lumped parameter approach, Int. J. Energy Res. 44 (6) (2020) 4516–4528.

[13]. Q. Cai, S. Zhu, The nexus between vibration-based energy harvesting and structural vibration control: a comprehensive review, Renew. Sustain. Energy Rev. 155(2022), 111920.1-111920.24.

[14]. J. Ke, J. Gao, Z.Y. Wu, Z. Xiang, X.D. Hu, Vari-stiffness characteristics of a 3D SMA hybrid basalt woven composite, Compos. Struct. 285 (2022), 115192.1- 115192.14.

[15]. Z. Zhang, J. Sun, L. Wang, J.J. Wei, Multiphysics-coupled study of wind load effects on optical performance of parabolic trough collector, Sol. Energy 207 (2020) 1078–1087.

[16]. C. Zhu, J. Yang, C. Rudd, Vibration transmission and energy flow analysis of L-shaped laminated composite structure based on a substructure method, ThinWalled Struct. 169 (2021), 108375.1-108375.20.

[17]. Z. Zhu, Z. Wang, K. Dai, X.F. Wang, H. Zhang, W.L. Zhang, An adaptive and space-energy efficiency vibration absorber system using a self-sensing and tunable magnetorheological elastomer, Nano Energy 117 (2023) 108927.